CHEMISTRY OF MATERIALS
Cite This: Chem. Mater. 2020, 32, 381−391
Article
pubs.acs.org/cm

Radioprotective Garment-Inspired Biodegradable Polymetal Nanoparticles for Enhanced CT Contrast Production

Johoon Kim,[†,‡] Alexander B. Silva,[‡] Jessica C. Hsu,[†,‡] Portia S. N. Maidment,[†] Nadav Shapira,[†] Peter B. Noël,[†] and David P. Cormode*[,†,‡,§]

[†]Departments of Radiology, [‡]Bioengineering, and [§]Medicine, Division of Cardiovascular Medicine, University of Pennsylvania, 3400 Spruce Street, 1 Silverstein, Philadelphia, Pennsylvania 19104, United States

Supporting Information

ABSTRACT: Numerous formulations of nanoparticle-based X-ray computed tomography (CT) contrast agents made of heavy metal elements are under investigation for their ability to provide improved CT imaging. Thus far, most experimental nanoparticle-based CT contrast agents have been developed with atoms of a single element. However, inspired by the composites formed from multiple elements used in radioprotective garments, we hypothesized that contrast agents made of several elements whose K-edge energies are spaced out in the high photon flux region could achieve high, broadband X-ray attenuation across the energies used in X-ray source spectra. Herein, we synthesized sub-5 nm core inorganic nanoparticles containing gold, tantalum, and cerium, and encapsulated them in polymeric nanoparticles to form polymetal nanoparticles (PMNP). We found that PMNP with multiple payload elements generate higher and more stable CT contrast than contrast agents made from a single contrast generating material, demonstrating the potential benefits of incorporating multiple suitable elements as CT contrast payloads.

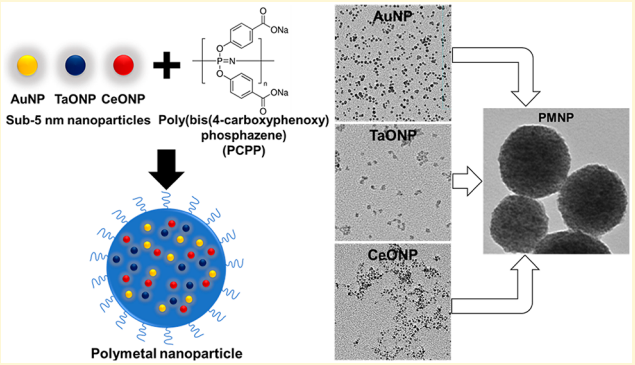

INTRODUCTION

As the field of nanomedicine has advanced, a myriad of nanoparticle formulations has been developed for imaging applications. Nanoparticle-based contrast agents for X-ray computed tomography (CT) imaging are no exception to this substantial research interest.[1−7] This interest stems from the numerous advantages of CT, such as high spatial and temporal resolution, fast acquisition time, no depth limit, and wide clinical availability. These inherent properties of CT have allowed it to become one of the most valuable instruments for cardiovascular imaging. However, current FDA-approved CT contrast agents for intravenous administration (i.e., iodinated small molecules) have several drawbacks. These drawbacks include short blood circulation times, which demand injection of high doses, shorten the imaging window, and increase the possibility of allergic reactions and renal toxicity.[8−10] The concern over contrast-induced nephropathy is particularly serious in patients with renal insufficiency. Because patients with cardiovascular diseases often have comorbid renal diseases,[11] there is a need to develop alternative CT blood pool contrast agents.

Despite the need, no new CT contrast agent has been approved for clinical use in nearly three decades;[12] however, this might soon change as numerous sizes, shapes, and structures of experimental CT contrast agents have been recently reported, complementing the rapid progression of CT technology in detectors and image reconstruction methods.[1,3,13] Most of these reports have focused on nanoparticles formed from dense, heavy metal elements, such as gadolinium, ytterbium, tantalum, gold, and bismuth.[14−19] Among nanoparticles made of these elements, gold nanoparticles (AuNP) are by far the most well-studied CT contrast agents, due to their favorable characteristics, including high elemental density of gold (d = 19.3 g/cm^3), excellent biocompatibility, and ease of control over its size, morphology, and surface chemistry.[20,21] However, gold is a relatively expensive material whose use could potentially increase the cost of CT imaging. Another heavy metal element that has been studied is tantalum.[7,18,22,23] Tantalum is also an appealing element for contrast agent development because of its high density (d = 16.4 g/cm^3) and its K-edge energy (67.4 keV) in a high photon flux region.[24] Moreover, a recent study from Kim et al. identified tantalum as one of the most viable elements for nanoparticle contrast agent development for CT imaging by demonstrating tantalum's high CT contrast production as compared to other candidate elements.[23] There exist many other candidate elements that may be suitable to be used as novel CT contrast agents. An element with potential, but has rarely been investigated for CT

Received: September 24, 2019
Revised: December 3, 2019
Published: December 4, 2019

DOI: 10.1021/acs.chemmater.9b03931
Chem. Mater. 2020, 32, 381−391

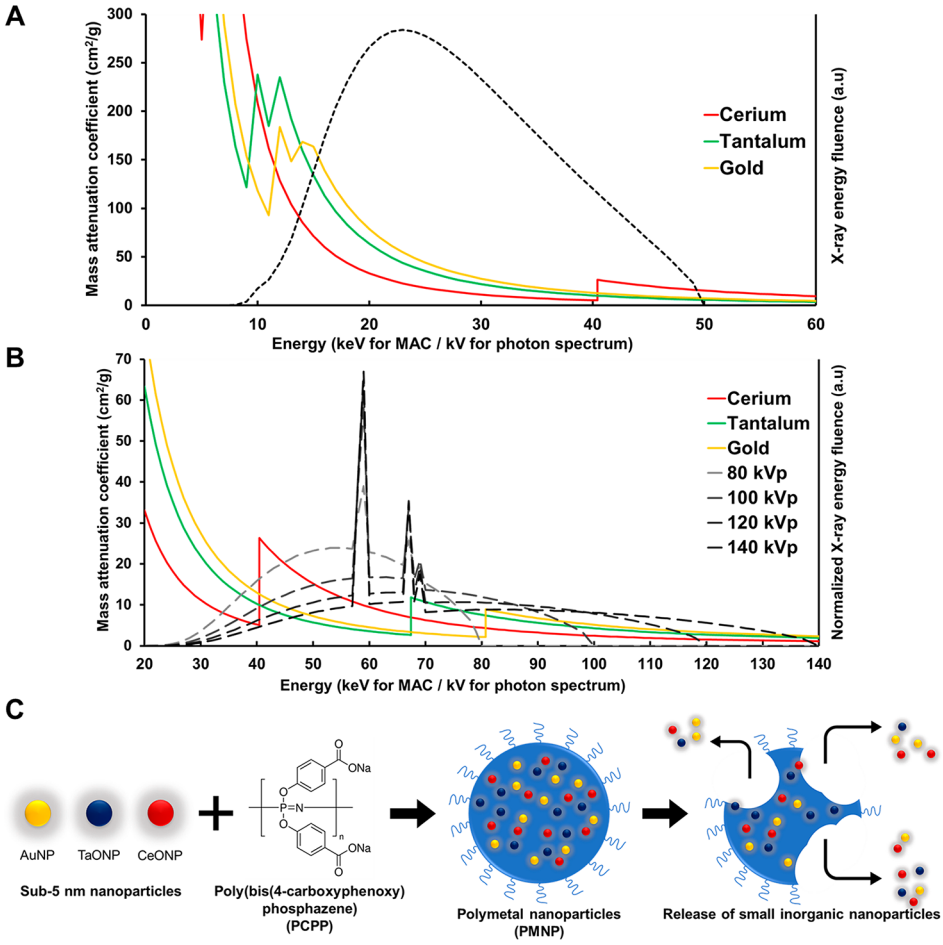

Figure 1. Contrast generating materials and structure of PMNP. Mass attenuation coefficient of cerium, tantalum, and gold and estimated X-ray photon spectra of (A) a MILabs μCT scanner at 50 kVp tube voltage and (B) a SOMATOM Force clinical CT scanner at 80, 100, 120, and 140 kVp. (C) Schematic depiction of PMNP formation and breakdown.

imaging, is cerium. Cerium also has its K-edge energy (40.4 keV) located in a high X-ray photon flux region, and cerium-based nanoparticles have been well-studied for numerous biomedical applications using their antioxidant activities and ROS scavenging abilities.[25−27]

Radioprotective garments worn by interventional radiologists are commonly known as lead clothing; however, they frequently contain a minority of lead, or no lead at all. This is because it is more effective in X-ray attenuation and lighter in weight to use composites of elements, such as tungsten, tin, barium, antimony, and bismuth, whose K-edges are spread through the range of energies used in medical imaging.[28,29] Inspired by such composite radioprotective garments, we hypothesized that an agent that incorporates multiple elements whose K-edges are spread over the diagnostic X-ray energy range might prove to have high contrast generation. The K-edge energies of the elements noted above (gold = 80.7 keV, tantalum = 67.4 keV, cerium = 40.4 keV) span the high photon flux regions of the X-ray spectra in the diagnostic range of tube voltage settings for μCT imaging (Figure 1A) and clinical CT imaging (Figure 1B). Moreover, tantalum and cerium are cheaper than some of the leading elements for CT contrast agent development, such as gold and platinum.[23] Thus, polymetal nanoparticles (PMNP) can potentially be lower in cost.

Our PMNP formulation is designed to encapsulate small gold, tantalum, and cerium nanoparticles that are sub-5 nm in core diameter in a larger polymer-based nanoparticle made of biodegradable poly di(carboxylatophenoxy)phosphazene (PCPP) (Figure 1B). PCPP belongs in a family of polymers known as polyphosphazenes, whose chemistry is defined by its phosphorus−nitrogen backbone. These polymers are well-studied for numerous biomedical applications, such as adjuvants for immunization and drug carriers, due to their excellent biocompatibility, tunability, and hydrophilicity.[30−32] These polymers are suitable for encapsulating small nanoparticles with hydrophilic coatings due to their hydrophilicity. They also slowly degrade into harmless hydrophilic byproducts, such as phosphate, tyrosine, ammonia, and 4-hydroxybenzoic acid, allowing PCPP-based nanoparticles to remain intact for several hours before degradation.[33] Our findings in this study suggest that our PMNP formulation can successfully encapsulate small sub-5 nm core inorganic nanoparticles made from gold, tantalum, and cerium. We have also shown that these PMNP are cytocompatible and biodegradable with robust CT contrast properties.

■ MATERIALS AND METHODS

Materials. Gold(III) chloride trihydrate (>99.9% trace metals basis), tantalum(V) ethoxide (99.98%), cerium(III) nitrate hexahydrate (99.99%), L-glutathione reduced, poly(acrylic acid), cyclohexane, IGEPAL CO-520, ammonium hydroxide solution (28.0−

DOI: 10.1021/acs.chemmater.9b03931
Chem. Mater. 2020, 32, 381−391

30.0% NH_3 basis), sodium hydroxide concentration (0.1 N), poly(bis(4-carboxyphenoxy)phosphazene) disodium salt (PCPP, 1 MDa), sodium borohydride, spermine tetrahydrochloride, and calcium chloride dihydrate were purchased from Sigma-Aldrich (St. Louis, MO). Herringbone microfluidic chip mixers were obtained from Microfluidic ChipShop (Jena, Germany). 2-(Carbomethoxy)-ethyltrimethoxysilane and 3-(trimethoxysilyl)propyl-*N*,*N*,*N*-trimethylammonium chloride were purchased from Gelest, Inc. (Morrisville, PA). Methoxy-poly(ethylene glycol)-*block*-poly(L-lysine hydrochloride) (PEG-PLL, PEG MW 5000, PLL MW 4900) was purchased from Alamanda Polymers (Huntsville, AL). HepG2, J774A.1, Renca, and SVEC4−10 cell lines were purchased from ATCC (Manassas, VA). LIVE/DEAD assay kits were acquired from Life Technologies Invitrogen (Grand Island, NY).

Gold Nanoparticle Synthesis. Gold nanoparticles were synthesized via a modified Turkevich method described by Cheheltani et al.[34] Briefly, gold(III) chloride salt in water was reduced by dropwise addition of sodium borohydride solution. After the mixture was stirred for 30 min, glutathione was added to the solution to cap the nanoparticle surface. The resulting solution was washed with deionized water three times in 10 kDa molecular cutoff centrifugation tubes and dispersed in PBS.

Tantalum Oxide Nanoparticle Synthesis. Tantalum oxide nanoparticles (TaONP) were synthesized by a modified reverse microemulsion method described by Kim et al.[23] Tantalum(V) ethoxide solution was added to 20 mL of cyclohexane-based microemulsion solution that contains 3 g of IGEPAL CO-520 and 75 mM NaOH solution. After 15 min, 250 uL of 2-(carbomethoxy)-ethyltrimethoxysilane and 500 uL of 3-(trimethoxyysilyl)propyl-*N*,*N*,*N*-trimethylammonium chloride were added to render the nanoparticle surfaces hydrophilic. A white sediment formed at the bottom of the flask after 24 h of stirring. After the colorless supernatant was carefully removed, the white sediment was dispersed in 5 mL of 5 M ammonium hydroxide solution and stirred for 30 min. Subsequently, 25 mL of ultrapure water was added, and the resulting solution was allowed to stir at room temperature for 2 h. The resulting solution was then centrifuged at 2500*g* for 30 min. The clear solution in the supernatant was further purified by centrifugation, washed with deionized water three times at 2500*g* for 30 min in 10 kDa molecular cutoff centrifugation tubes, and dispersed in PBS.

Cerium Oxide Nanoparticle Synthesis. Small cerium oxide nanoparticles (CeONP) were synthesized by modifying an alkaline-based precipitation method described by Perez et al.[35] 217 mg of cerium nitrate hexahydrate salt dissolved in 4 mL of deionized water was mixed with 50 mg of poly(acrylic acid) polymer dissolved in 2 mL of deionized water. The resulting mixture was then added to 100 mL of 0.4 M ammonium hydroxide solution. After being stirred for 24 h, the solution turned from turbid light brown to clear yellow. The resultant nanoparticle solution was centrifuged at 2600*g* for 30 min, and the yellow supernatant was collected. The supernatant was then washed with deionized water four times in 10 kDa molecular cutoff centrifugation tubes and suspended in PBS.

PCPP Formulations and PMNP Synthesis. PCPP nanoparticles were synthesized on the basis of a method previously reported by Cheheltani et al.[34] In this method, 2 mL of 0.1% (w/v) PCPP solution and 2 mL of 0.01% (w/v) spermine solution that also contains 1.45 uL of 3.5% PEG-PLL (0.05 mg) were both prepared in PBS. The pH levels of these solutions were adjusted to 7.4 before loading each solution in a 10 mL syringe. Subsequently, both solutions were flowed through a herringbone mixer microfluidic chip at a flow rate of 6 mL/min. The resultant output solution was then quickly added to 100 mL of 8.8% (w/v) $CaCl_2$ solution. After being stirred for 20 min, the solution was purified by centrifugation at 550*g* for 7 min in DI water three times. To encapsulate small nanoparticles in PCPP, desired amounts of AuNP and CeONP were added to the PCPP solution, and TaONP was added to the spermine and PEG-PLL solution before loading them in the syringes. The amounts of added PEG-PLL were varied from 0 to 0.2 mg to synthesize PMNP of varying sizes.

Nanoparticle Characterization. Transmission electron microscopy (TEM) was used to determine the core sizes and morphologies of the core metal nanoparticles and PCPP nanoparticles. The images were acquired using a Tecnai T12 microscope (FEI, Hillsboro, OR) or a JEOL 1010 microscope (JEOL Ltd., Tokyo, Japan). Diameters of 500 individual nanoparticles of each formulation were manually measured on TEM images using ImageJ. The hydrodynamic diameter and zeta potential of the nanoparticles were assessed by using a Nano-ZS-90 Zetasizer (Malvern Instruments, Worcestershire, UK) by preparing the samples at 0.2 mg/mL in concentration. The concentrations of the elemental payloads in the nanoparticles were measured by using ICP-OES (Spectro Analytical Instruments GmbH, Kleve, Germany).

EDS Elemental Mapping. Energy-dispersive X-ray spectroscopy (EDS) imaging was used to investigate the encapsulation of the metal nanoparticles of all three elements and their spatial distribution in an individual PMNP. A FEI Quanta 600 Environmental scanning electron microscope (FEI, Hillsboro, OR) equipped with a Bruker Quantax Silicon Drift Detector for EDS analysis was used. The samples were prepared on copper grids. M-edge energy mappings were used for the presence of gold and tantalum, and L-edge energy mapping was used for the presence of cerium in the field of view. A mixed population of single metal PCPP nanoparticles (SMNP), each encapsulating AuNP, TaONP, or CeONP, was used as a control to confirm the accuracy of elemental mapping at the imaging magnification.

In Vitro PCPP Nanoparticle Degradation and Core Metal Nanoparticle Release. PMNP and SMNP (AuPCPP represents AuNP encapsulating PCPP nanoparticles, TaPCPP represents TaONP encapsulating PCPP nanoparticles, and CePCPP represents CeONP encapsulating PCPP nanoparticles) formulations at their maximum loading capacities were added to 2 mL of PBS containing 10% fetal bovine serum at a concentration of 0.15 mg/mL in payload elements (e.g., gold, tantalum, and cerium in PMNP and gold in AuPCPP). The solutions were continuously flowed through platinum cured silicon tubing that was 1.42 mm in internal diameter via a FH100M multichannel peristaltic pump (Fisher Scientific, Hampton, NH) at a volumetric flow rate of 5 mL/min. At days 1, 2, 4, and 7 of dynamic incubation, the solutions were collected and centrifuged at 500*g* for 5 min. The concentrations of gold, cerium, and tantalum in the supernatant and the pellet were analyzed via ICP-OES to evaluate the release of small metal nanoparticles at each time point. The amounts of released nanoparticles were calculated by dividing the concentration measured in the supernatant by the concentrations measured in both the supernatant and the pellet. The samples were prepared in triplicate. TEM images of partially degraded PMNP were also acquired to confirm the release of core nanoparticles.

In Vitro Safety and Cytotoxicity. The LIVE/DEAD assay was used to evaluate the safety and cytotoxicity of the core nanoparticles and the PCPP formulations with HepG2 (hepatocytes), Renca (epithelial kidney cells), and SVEC4-10EHR1 (endothelial cells). The cells were cultured in accordance with ATCC recommendations. 1.0 × 10^5 cells were seeded in each well of 24-well plates and were cultured for 24 h at 37 °C and 5% CO_2. After 24 h of culture, the medium was removed and replaced with fresh medium that contains the payload elements of a range of concentrations (i.e., 0.025 mg Au/mL to 1 mg Au/mL for AuNP and AuPCPP). The cells were incubated with the nanoparticle-treated media for 8 h before they were washed with DPBS and treated with LIVE/DEAD stain (4 uL of 3.2 mM Hoechst 33343, 1 uL of calcein AM, and 2 uL of ethidium homodimer-1 in 2 mL of DPBS) for 20 min. The stained cells were imaged with a fluorescence microscope. Images of cell nuclei, live cells, and dead cells were acquired at four different fields of view in each well, and the numbers of live and dead cells were counted to calculate the cell viability in percentage (viability % = live cell count/total cell count). The experiment was repeated three times for each cell line for a total of 12 measurements per data point (n = 3, field of view = 4).

In Vitro Phantom CT Imaging. Each PCPP formulation was suspended in 1% agar gel at concentrations of 0, 0.5, 1, 2, 4, 6, and 8

DOI: 10.1021/acs.chemmater.9b03931
Chem. Mater. 2020, 32, 381−391

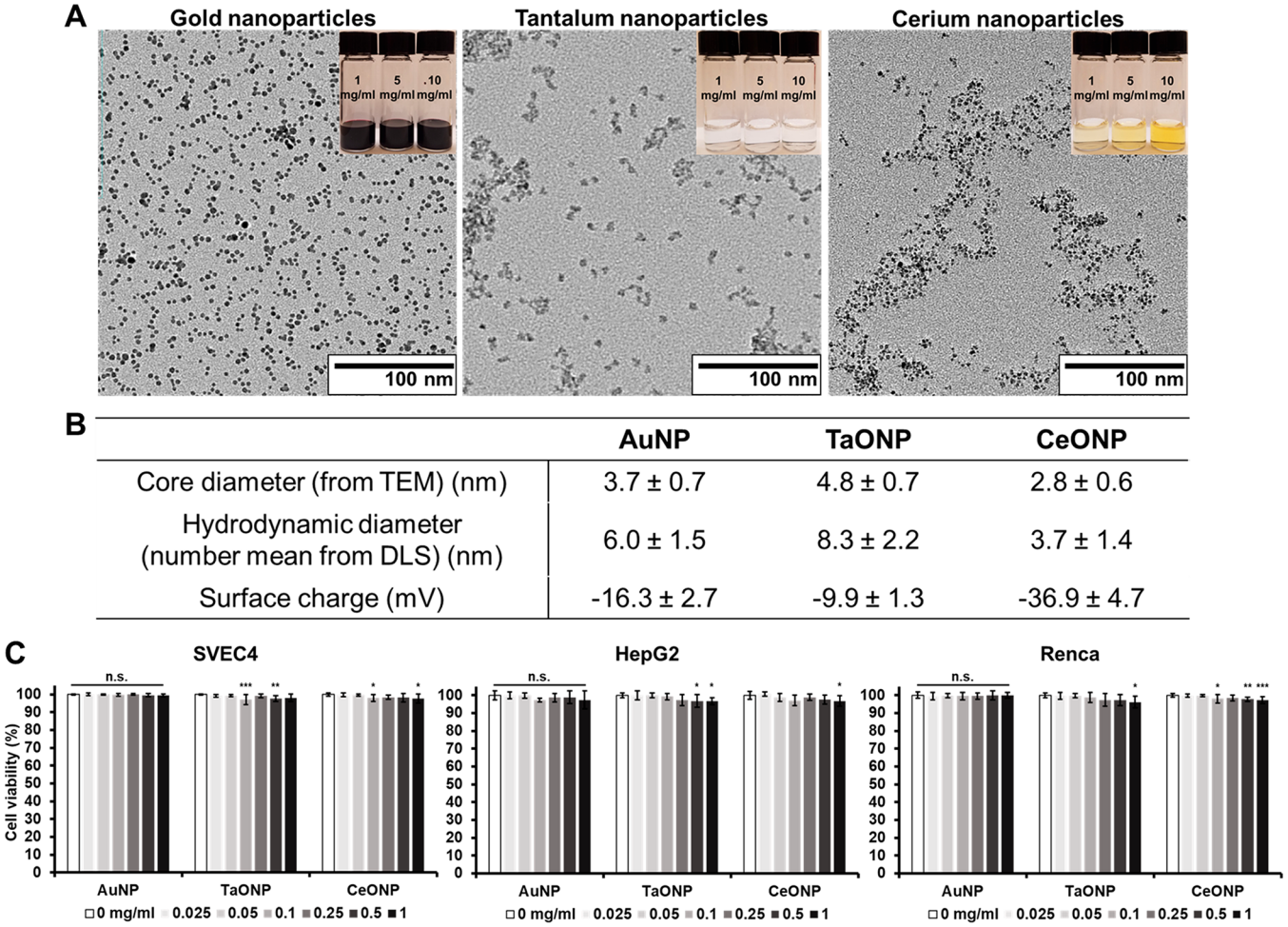

	AuNP	TaONP	CeONP
Core diameter (from TEM) (nm)	3.7 ± 0.7	4.8 ± 0.7	2.8 ± 0.6
Hydrodynamic diameter (number mean from DLS) (nm)	6.0 ± 1.5	8.3 ± 2.2	3.7 ± 1.4
Surface charge (mV)	-16.3 ± 2.7	-9.9 ± 1.3	-36.9 ± 4.7

Figure 2. Characterization of small core metal nanoparticles of PMNP. (A) TEM of small core metal nanoparticles and photos of the corresponding nanoparticles at concentrations of 1, 5, and 10 mg/mL (top right insets). (B) The core and hydrodynamic diameters and surface charge of the small core metal nanoparticles. (C) Normalized cell viability of SVEC4, HepG2, and Renca after 8 h of incubation with AuNP, TaONP, and CeONP (n.s. = not significant or $p > 0.05$, * = $p \leq 0.05$, ** = $p \leq 0.01$, *** = $p \leq 0.001$ as compared to the control group (0 mg/mL)).

mg/mL ($n = 3$ per concentration). Each sample was prepared in a 0.2 mL flat cap microcentrifuge tube. These samples were secured in a plastic rack along with a tube containing water and a tube containing no solution (or air) for μCT imaging. μCT imaging was performed using a MILabs μCT scanner (MILabs, Utrecht, The Netherlands). The images were acquired using a standard protocol with 0.1 mm beryllium and 0.5 mm aluminum filtration, tube voltage of 50 kVp, tube current at 0.24 mA, step angle of 0.75°, and exposure time of 75 ms. The identical samples were loaded in a custom-made, acrylonitrile butadiene styrene tube holder that is designed to fit in the borehole of an anthropomorphic thorax phantom body (QRM GmbH, Mohrendorf, Germany) for imaging with a SOMATOM Force clinical CT scanner (Siemens Healthineers, Erlangen, Germany). The phantom body mimics human organs in the thorax in terms of density, CT attenuation, and size (200 × 300 × 200 mm). The CT images were acquired using a customized protocol adapted from Siemens original adult abdomen routine imaging protocol at 80, 100, 120, and 140 kVp. The following parameters were used: beam filtration of 0.3 mm titanium and 0.5 mm aluminum, anode angle of 8°, scan mode of helical acquisition, X-ray tube current of 360 mA, exposure time of 0.5 s, slice thickness of 0.5 cm, and field of view of 370 × 370 mm. For both μCT and CT imaging, the images were analyzed using OsiriX software (Pixmeo, Bernex, Switzerland). Circular ROIs were drawn on five different axial planes of each tube. The mean attenuation values from 15 slices for each concentration (five slices × three tubes) were recorded and normalized to the values from our control tubes with 1% agar gel (i.e., 0 mg/mL solution). Attenuation rate was defined by the slope of the linear regression line that models the relationship between attenuation and elemental concentration in either milligram/milliliter or millimolar.

Simulation of Relative Contribution of PMNP Payload Elements in CT Imaging. A custom-written Python code was used to estimate the relative contribution from each payload element to the CT attenuation of PMNP under imaging conditions used in this study (i.e., 50 kVp in μCT imaging and 80, 100, 120, and 140 kVp in clinical CT imaging). In this model, CT attenuation of PMNP is calculated using National Institute of Standards and Technology (NIST) elemental attenuation values of materials in the PMNP samples (i.e., water, PCPP polymer, gold, tantalum, and cerium), density of payload elements (i.e., gold, tantalum, and cerium), and estimated X-ray source spectra (beam filtration of 0.1 mm beryllium + 0.5 mm aluminum for μCT imaging and 0.3 mm titanium + 0.5 mm aluminum for clinical CT imaging) used in our imaging studies, from which the relative contribution in PMNP's attenuation from each element is calculated.

In Vivo Mice Imaging. All animal experiments were performed in accordance with the protocols approved by University Laboratory Animal Resources in conjunction with the Institutional Animal Care and Use Committee at the University of Pennsylvania. In vivo CT images were acquired from a MILabs μCT scanner, using the same scanning parameters from the phantom imaging. After acquiring

DOI: 10.1021/acs.chemmater.9b03931
Chem. Mater. 2020, 32, 381−391

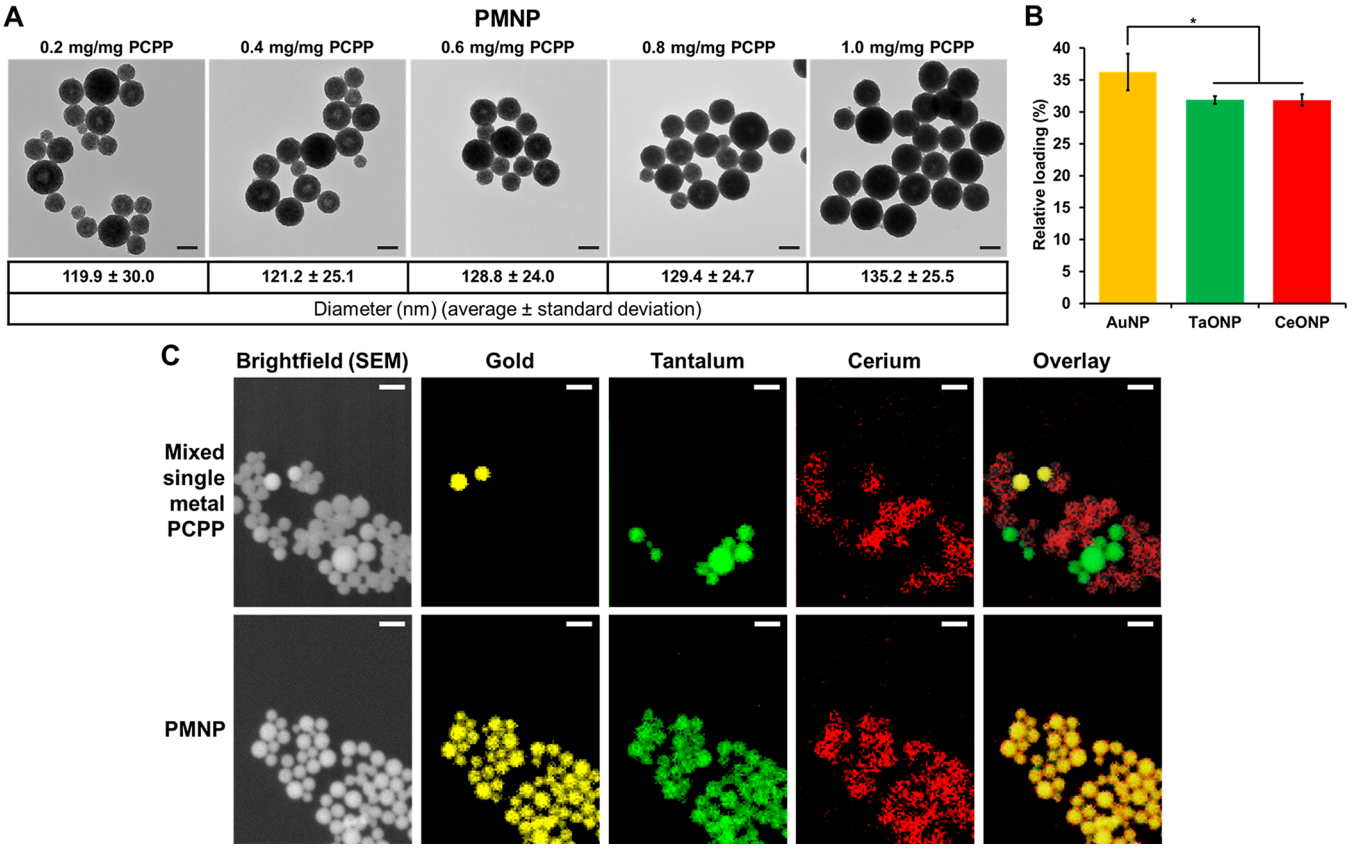

Figure 3. Encapsulation of small core nanoparticles in PMNP. (A) TEM of PMNP with various loadings of core nanoparticles. Scale bar = 100 nm. (B) Relative percentages of each payload at maximum loading in PMNP (1 mg Au,Ta,Ce/mg PCPP) (* = $p \leq 0.05$). (C) SEM brightfield images, EDS mappings of gold, tantalum, and cerium, and overlay images. Scale bar = 200 nm.

prescan images, C57BL/6J mice were injected with either 40 μL of PMNP ($n = 3$) or AuPCPP ($n = 3$) containing 0.1 mg of the payload (i.e., gold in AuPCPP and gold, tantalum, and cerium combined for PMNP) and were scanned again immediately after postinjection. Both formulations were injected in the left thigh muscle of the mice. The acquired images were subsequently analyzed with Osirix. Using a 3D region growing segmentation function, 3D regions of interest (ROI) that enclosed the injection sites were isolated and highlighted. The total attenuation that was generated by either AuPCPP or PMNP was quantified by addition of the attenuation values (in Hounsfield Unit) of each voxel within the 3D ROI and subtraction of the total attenuation generated by the soft tissue in the left thigh muscle from the preinjection scan from this number.

Statistical Analysis. The slope (m_χ) and the standard error of fit (e_χ) of attenuation rates from μCT and CT were calculated using the least-squares method of linear regression. One-way analysis of variance (ANOVA) was used to test if there is an overall difference between the groups in safety and cytotoxicity, payload loading ratio, biodegradability, and attenuation rates. In cases in which the p-value from the ANOVA test indicated that there is an overall significant difference between the groups ($p \leq 0.05$), Tukey−Kramer HSD (honestly significant difference) posthoc test was used to confirm which specific pairs of groups had significant differences. A two-sample t test was used to compare total attenuation generated by PMNP and AuPCPP from in vivo imaging. Error bars in the graphs represent one standard deviation unless indicated otherwise.

■ RESULTS

AuNP, TaONP, and CeONP Characterization and In Vitro Safety and Cytotoxicity. Small core nanoparticles, AuNP, TaONP, and CeONP, were synthesized and capped with ligands that provide hydrophilicity and stability in biological fluids. The core sizes of AuNP, TaONP, and CeONP were determined to be 3.7 ± 0.7, 4.8 ± 0.7, and 2.8 ± 0.6 nm, respectively, while their hydrodynamic diameters were slightly larger in each case (Figure 2A,B). The zeta potentials of AuNP and TaONP that were both capped with ligands of zwitterionic charges were closer to neutral when compared to that of CeONP, which was capped with negatively charged poly(acrylic acid).

The safety and cytotoxicity of these small metal nanoparticles were then assessed by incubating them with cell types that would likely have the highest exposure upon intravenous injection (i.e., endothelial cells (SVEC4-10EHR1), liver hepatocytes (HepG2), and kidney cells (Renca)) for 8 h. While there were statistically significant differences for some of the treatment concentrations for TaONP and CeONP for all cell types when compared to the control groups (0 mg/mL), the lowest cell viability observed was 96.2 ± 3% (for Renca cells incubated with TaONP at 1.0 mg Ta/mL), indicating that the reductions were not substantial (Figure 2C). These results justified the use of these nanoparticles in the next steps of this study.

Encapsulation of Small Core Nanoparticles in PCPP Nanoparticles. The aforementioned AuNP, TaONP, and CeONP formulations were successfully incorporated into PCPP nanoparticles either individually to form SMNP or jointly to form PMNP. We assessed the loading capacity of both SMNP and PMNP that are synthesized with addition of 25 μg PEG-PLL/mg PCPP (which results in unloaded PCPP nanoparticles with an average diameter of 102.4 nm). In the case of AuPCPP, more than 5 mg of gold payload could be

DOI: 10.1021/acs.chemmater.9b03931
Chem. Mater. 2020, 32, 381−391

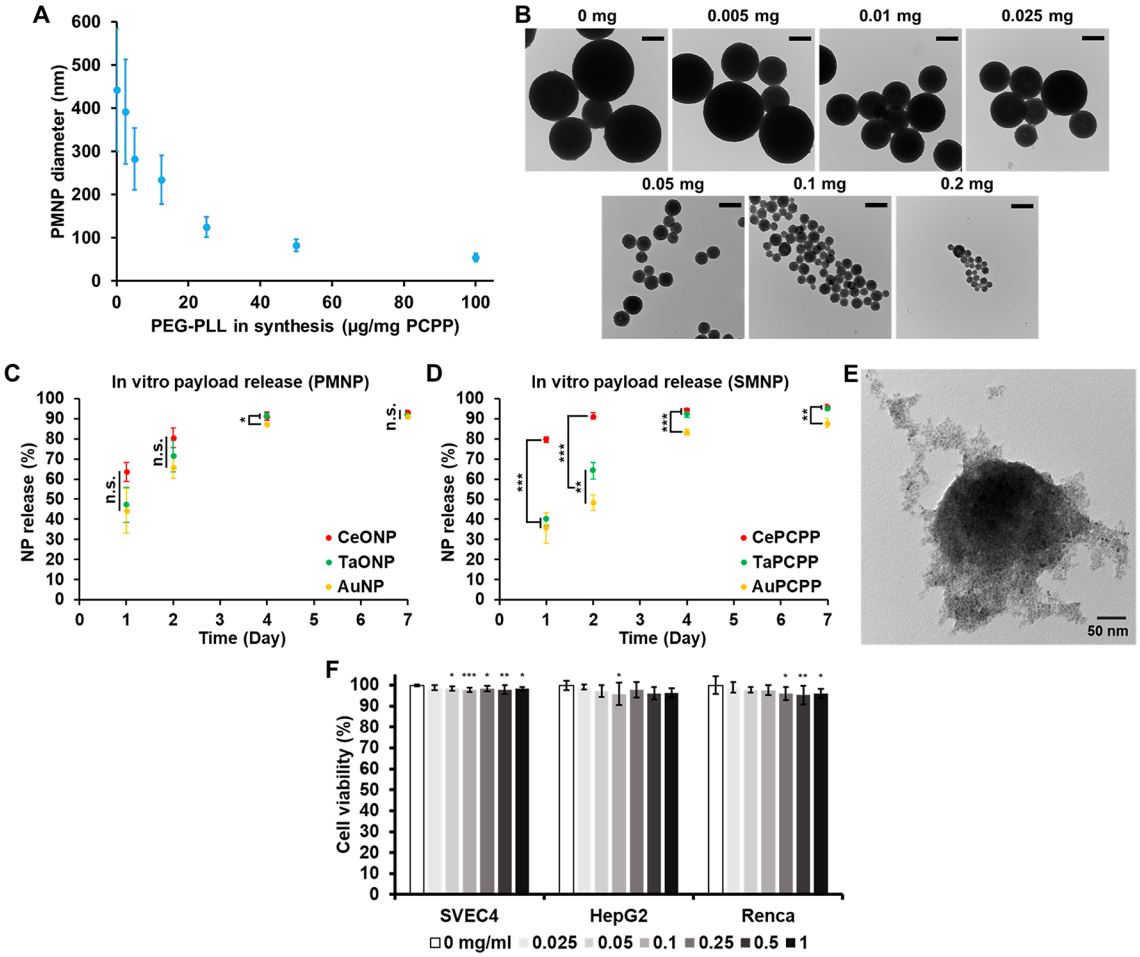

Figure 4. In vitro properties of PMNP. (A) Effect of PEG-PLL on PMNP diameter. (B) TEM of PMNP of different sizes. Scale bar = 200 nm. Payload release from (C) PMNP and (D) SMNP. (E) TEM of partially degraded PMNP after 4 days of dynamic incubation (n.s. = not significant or $p > 0.05$, * = $p \leq 0.05$, ** = $p \leq 0.01$, *** = $p \leq 0.001$). (F) Effect of PMNP on cell viability after 8 h of incubation (* = $p \leq 0.05$, ** = $p \leq 0.01$, *** = $p \leq 0.001$ as compared to the control group (0 mg/mL)).

encapsulated per milligram of PCPP polymer used during the synthesis without deviation from spherical morphology (Figure S1A). Similarly, up to 1.25 mg of tantalum and 0.375 mg of cerium per milligram of PCPP could be loaded in their corresponding SMNP formulations (Figure S1B,C). Less tantalum and cerium incorporation can be explained by their lower elemental densities (d_{Ta} = 16.6 g/cm^3, d_{Ce} = 6.8 g/cm^3) when compared to the density of gold (d_{Au} = 19.3 g/cm^3) and the presence of other constituents in the core of TaONP and CeONP (i.e., oxygen atoms). When AuNP, TaONP, and CeONP at equal concentrations were encapsulated collectively to form PMNP, a maximum of 1 mg of total payload (gold + tantalum + cerium) per milligram of PCPP polymer could be loaded without disrupting the morphology (Figure 3A and Figure S2). At the maximum loading capacity, the mean diameter of PMNP increased by 35% when compared to that of nonloaded PCPP nanoparticles (Figure S3). As seen for both SMNP and PMNP, incorporation of higher payloads increased the diameter of PCPP nanoparticles.

Although the ratio of incorporated payloads of different elements can be freely adjusted, the PMNP formulations reported herein were synthesized with 1:1:1 ratios of gold:tantalum:cerium payloads. To assess the relative ratios of these elements encapsulated in PMNP, their concentrations were analyzed by ICP-OES. As shown in Figure 3B, the ratios of elements loaded in PMNP were similar to the input ratios.

Spatial Distribution of Small Core Nanoparticles in PCPP Nanoparticles. PMNP was analyzed with EDS mapping to investigate the encapsulation of all three elements further and to examine the spatial distribution of these elements in individual PMNP. To ensure the accuracy of elemental mapping, we used a mixed population of SMNP as a control. As seen in Figure 3C, SMNP loaded with either gold, tantalum, or cerium could be successfully differentiated from one another in our control group. Each element was located in its corresponding SMNP formulation without any overlap, allowing us to identify the loading element in each SMNP accurately. On the other hand, for PMNP, all three elements were detected in every PCPP nanoparticle. The elemental maps were colocalized to the location of PCPP nanoparticles in the brightfield image in both groups as well. These data suggest successful coencapsulation of all three small core nanoparticles into each individual PMNP.

Size Control of PMNP. As demonstrated in Figure 4A,B, the size of PMNP (0.5 mg Au,Ta,Ce/mg PCPP) could be controlled in the range of 50−450 nm by varying the amount of PEG-PLL used in the synthesis from 0 to 0.2 mg per milligram of PCPP. The average diameter of PMNP decreased with increasing amounts of PEG-PLL in a nonlinear manner.

DOI: 10.1021/acs.chemmater.9b03931
Chem. Mater. 2020, 32, 381−391

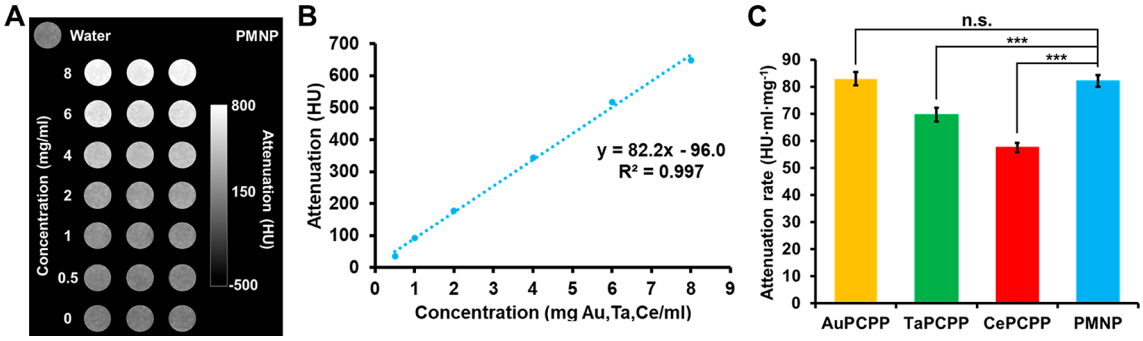

Figure 5. In vitro contrast generation of PMNP and SMNP in μCT imaging. (A) Phantom image of PMNP from a MILabs μCT system. (B) Attenuation of PMNP at a range of concentrations. (C) Attenuation rates of different PCPP formulations (n.s. = not significant or $p > 0.05$, *** = $p \leq 0.001$). Phantom images of SMNP formulations are provided in Figure S5.

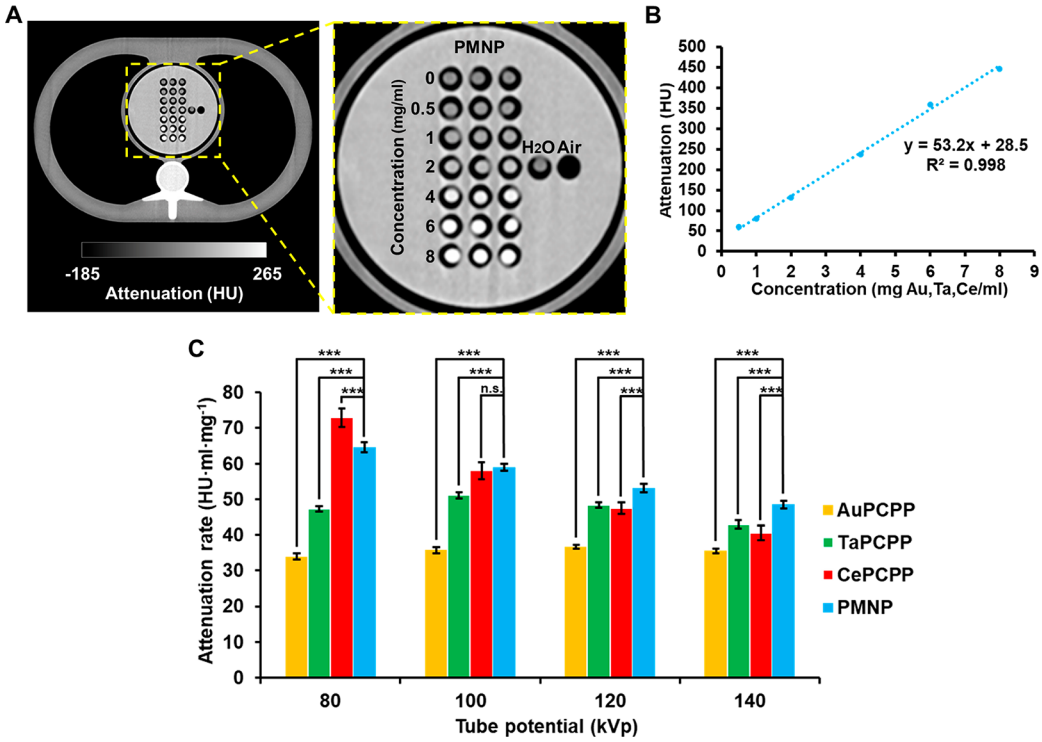

Figure 6. In vitro contrast generation of PMNP and SMNP in clinical CT imaging. (A) Phantom image of PMNP samples from a SOMATOM Force CT scanner, and an enlarged image of the phantom centered at the PMNP samples. (B) Attenuation of PMNP at a range of concentrations. (C) Attenuation rates of different PCPP formulations at different tube voltage settings derived from a clinical CT scanner (n.s. = not significant or $p > 0.05$, *** = $p \leq 0.001$). Phantom images of SMNP formulations are provided in Figure S6.

As reported in our previous study with nonloaded PCPP nanoparticles, addition of PEG-PLL limits the growth of PCPP nanoparticles with the presence of more PEG-PLL resulting in smaller PCPP nanoparticles.[34]

In Vitro Biodegradability of PMNP. For eventual excretion of PMNP, the small core nanoparticles in PMNP would need to be released from their polymeric components effectively. We therefore evaluated the release rate of the core nanoparticles by incubating PMNP in 10% fetal bovine serum in PBS at 37 °C for 1, 2, 4, and 7 days. The PMNP solution was constantly flowed through a tubing during the incubation periods to mimic the dynamic nature of blood and interstitial fluid. We observed that approximately 90% of AuNP, TaONP, and CeONP was released from PMNP in 7 days, demonstrating the degradability of PMNP and the effective release of its core nanoparticles (Figure 4C). Unlike SMNP formulations that showed clear differences in the release pattern of their core nanoparticles (Figure 4D), the release rates of the three core nanoparticle formulations in PMNP were comparable to each other, indicated by much smaller statistical differences throughout the time of the study. More rapid release of CeONP from CePCPP can be explained by the smaller hydrodynamic diameter of CeONP and possibly their strong negative surface charge. TEM of partially degraded PMNP confirmed the dissociation and the release of core nanoparticles from PMNP (Figure 4E).

In Vitro Safety and Cytotoxicity of PMNP. The safety and cytotoxicity of PMNP as well as of AuPCPP, TaPCPP, and CePCPP were evaluated using the same method used to assess the safety and cytotoxicity of the small core nanoparticles (Figure 4F and Figure S4). Once again, incubation of the selected cell lines with PMNP and SMNP formulations for 8 h

DOI: 10.1021/acs.chemmater.9b03931
Chem. Mater. 2020, 32, 381−391

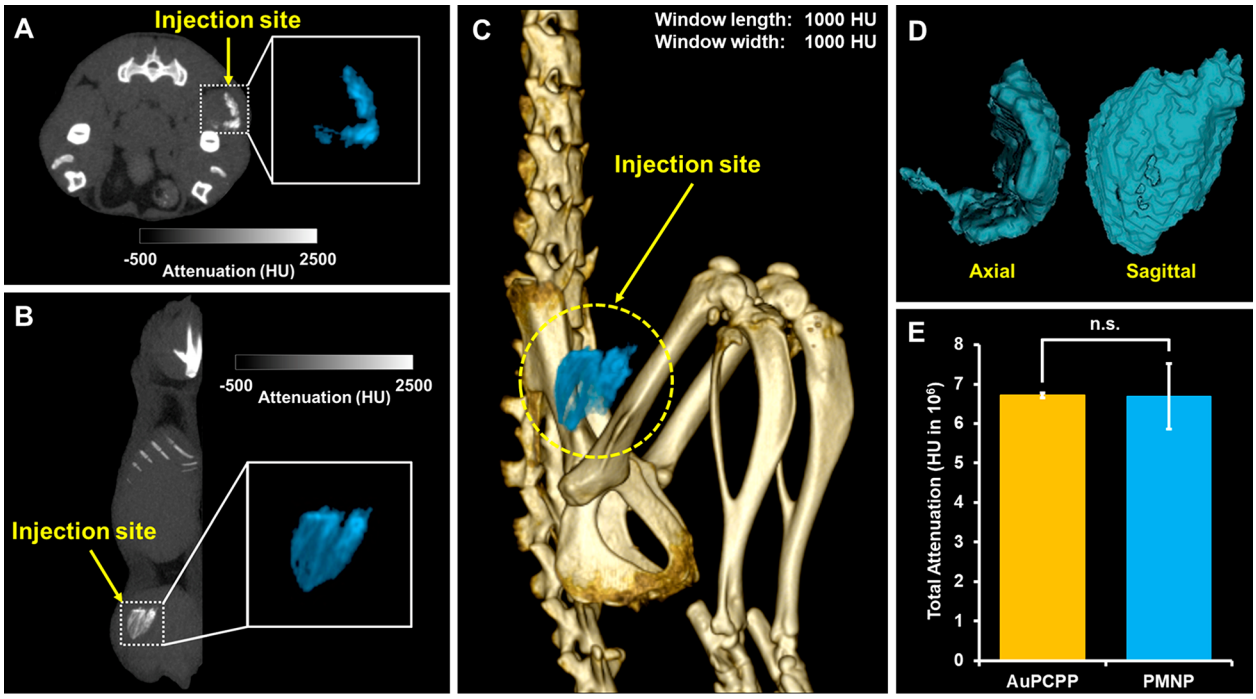

Figure 7. In vivo images and contrast generation analysis. CT images of PMNP injected in the thigh muscle viewed in the (A) axial plane and the (B) sagittal plane. Insets represent enlarged images of injected PMNP highlighted in light blue. (C) 3D rendered CT image of a mouse with the PMNP injection site highlighted in light blue. (D) Isocontour depiction of injected PMNP in both axial and sagittal views. (E) Image analysis of the attenuation arising from nanoparticle injections (n.s. = not significant).

did not considerably affect cell viability when compared to the control groups (0 mg/mL). The lowest mean cell viability observed from PMNP incubation was 96 ± 2% in Renca cell line at a treatment concentration of 1 mg Au,Ta,Ce/mL. The results of high cell viability from both small core nanoparticles and PCPP formulations suggest that PCPP polymer and its byproducts do not have significant cytotoxicity, which agrees with previous findings on nanoparticles formed from this polymer.[34,36,37]

Contrast Generation of PMNP in microCT and Clinical CT Imaging. We next assessed PMNP's CT contrast properties using both a μCT scanner and a clinical CT scanner. A MILabs μCT scanner with a tube voltage of 50 kVp was used to scan both SMNP and PMNP solutions of increasing element concentration (e.g., gold in AuPCPP and gold, cerium, and tantalum combined in PMNP) (Figure 5A and Figure S5). All of the formulations, AuPCPP, TaPCPP, CePCPP, and PMNP, had linear correlations between the attenuation and the concentration, with R^2 values >0.99 in each case (the data for PMNP are shown in Figure 5B as an example). From the attenuation rate measurements, we found that PMNP and AuPCPP had the highest values, followed by TaPCPP and CePCPP. The attenuation rate of PMNP was not statistically significantly different from that of AuPCPP (Figure 5C).

The same PCPP formulations were scanned in a SOMATOM Force clinical CT scanner at four different tube voltages of 80, 100, 120, and 140 kVp. The solutions were scanned in an anthropomorphic phantom body that closely mimics the thorax of a patient (20 cm × 30 cm × 20 cm) to improve the clinical relevance of the data. An axial plane image of the phantom body containing PMNP and SMNP solutions at a tube voltage of 120 kVp is shown in Figure 6A and Figure S6, in which the increase in attenuation is clearly observed with increasing concentration of the payload. In validation of the images, an excellent linear correlation between the attenuation and the concentration was observed (Figure 6B). As expected, we observed that the attenuation rates of both SMNP and PMNP depended heavily on the tube voltage (Figure 6C).

The attenuation rates of AuPCPP were the lowest across all four tube voltages in this study. The attenuation rates of TaPCPP remained higher than those of AuPCPP across all tube voltages. TaPCPP's attenuation rate slightly increased from 80 to 100 kVp before decreasing again at higher tube voltages of 120 and 140 kVp. Unlike AuPCPP and TaPCPP, a steep decrease in attenuation rate was observed for CePCPP with increasing tube voltage. Its attenuation rate was the highest at 80 kVp; however, due to cerium's comparatively low K-edge energy of 40.4 keV, the attenuation rate sharply decreased to lower than that of TaPCPP at 140 kVp. Interestingly, PMNP also exhibited a decline in attenuation rate with increasing tube voltage. However, the rate of decline was much lower than that of CePCPP, which resulted in its attenuation rate being the second highest after CePCPP at 80 kVp to being the highest in both 120 and 140 kVp. Similar trends were observed when attenuation rates were calculated on the basis of molar concentration of the PCPP formulations. Notably, the attenuation rates of PMNP were higher than those of other formulations across all tube voltages used in our study with the exception of TaPCPP at 120 kVp (Figure S7).

Relative CT Attenuation Contribution by Each Payload Element in PMNP. Using NIST attenuation coefficients of gold, tantalum, and cerium and X-ray source energy spectra, we calculated the attenuation that was produced by each payload element in PMNP. The relative attenuation contributions from each payload elements were comparable to the ratios of differences in attenuation rates between SMNP formulations in our in vitro imaging study (Figure S8).

DOI: 10.1021/acs.chemmater.9b03931
Chem. Mater. 2020, 32, 381−391

Attenuation from gold was the largest followed by tantalum and cerium, respectively, in 50 kVp used in μCT imaging simulation. The relative attenuation ratio of cerium decreased and those of gold and tantalum slowly increased as the tube potential increased in clinical CT imaging simulation. Interestingly, the relative ratios of contribution between gold and tantalum were very similar to one another across all tube potentials used in this study.

In Vivo Contrast Generation of PMNP. In vivo contrast properties of PMNP were assessed by imaging mice that were intramuscularly injected with the same dose and volume (0.1 mg, 40 μL) of either PMNP or AuPCPP that showed the highest attenuation rates in μCT phantom imaging. As shown in Figure 7A−C, the ROI of contrast agents surrounding the injection site were isolated and highlighted in both 2D and 3D images, due to production of strong CT contrast by these contrast agents. The highlighted area could also be accurately depicted in 3D isocontour mapping for better visualization of its volume (Figure 7D). To quantify and compare the contrast generation by PMNP and AuPCPP, total attenuation (summation of CT attenuation values in each voxel) of the isolated 3D ROI was measured. In agreement with comparable attenuation rates between PMNP and AuPCPP observed in μCT phantom imaging, the total attenuation generated by PMNP had no statistically significant difference from the total attenuation measurement of AuPCPP (Figure 7E).

■ DISCUSSION

In this study, by encapsulating small core nanoparticles made of three different elements (gold, tantalum, and cerium) in PCPP polymer, we developed biodegradable polymetal nanoparticles that can generate high CT contrast at various tube voltage settings used in both μCT and clinical CT scanners. Our phantom and in vivo mice imaging study results both support that contrast agents made of several elements whose K-edge energies are spread out within the high flux photon region can generate consistently high attenuation in CT imaging of various X-ray source spectra as compared to contrast agents whose payload is based on a single element, similar to the effects observed in radioprotective garments. In fact, our PMNP formulation generated significantly higher attenuation than well-studied experimental CT contrast payload materials, such as gold and tantalum alone, in different tube potential settings used in this study. The attenuation rates of PMNP observed in our study are also much higher than those of an iodinated contrast agent (i.e., iopamidol) reported by Hsu et al.,[38] who acquired the data with the identical CT scanner, tube voltage, and other scanning parameters used in our study. The high attenuation generation of our PMNP formulation throughout low and high tube voltage settings can offer an advantage over use of payload elements of low K-edge energies, such as cerium and commonly used iodine in numerous CT imaging applications. These low K-edge energies suffer from deterioration of attenuation generation at high tube voltage (e.g., 140 kVp),[39] which indicates that our PMNP formulation can especially be beneficial in CT imaging of obese patients, a rapidly growing patient pool,[40] which often requires imaging at high tube voltage.[41,42] Most studies of novel CT contrast agent development focus on either small molecules or nanoparticles made of single element payloads. However, the observations made in this study indicate that the development of CT contrast agents with two or more CT payload elements can potentially improve their CT contrast properties. Future investigation of the amount, ratio, and identification of different payload elements (e.g., gadolinium and ytterbium) will further enhance the CT contrast properties of PMNP. As shown in our simulation, ideal ratios and choices of payload elements can be predicted with sufficient accuracy to make PMNP suitable for user-specific CT imaging applications.

In our design of PMNP, we have loaded the hydrophilic core nanoparticles in PCPP polymers. However, various kinds of platforms capable of acting as carriers for multiple contrast generating materials are available. These platforms include micelles, liposomes, nano- and microemulsions, dendrimers, lipoproteins, and other polymeric nanoparticles (e.g., PLGA, alginate), all of which have previously been demonstrated to be effective carriers of contrast payloads.[43−48] Many of these platforms, such as liposomes and lipoproteins, are also capable of containing both hydrophilic and hydrophobic payloads, further expanding the choices of payload materials for the synthesis of polymetal nanoparticles.

Our previous studies have loaded inorganic nanoparticles in PCPP nanoparticles.[34,49] However, this study was the first attempt to include core nanoparticles of three different elements, which can lead to increased affordability as compared to other leading experimental CT contrast agents (e.g., AuNP), reduced dose-related cytotoxicity, and, most importantly, improved CT attenuation production. As mentioned above, the potential for PMNP to be a contrast agent with excellent CT contrast properties has been demonstrated. However, future work is needed to develop PMNP into a blood pool agent with desired pharmacokinetics and sufficient excretion of its payloads. The possibility of achieving sufficient excretion is promising, considering the versatility of PCPP-based nanoparticles. By adjusting the amount of PEG-PLL added, the diameter of PMNP could be controlled. The side-chain groups and the molecular weight of PCPP can also be readily adjusted, allowing us to control PMNP's degradation rate and its diameter at ease.[50] Other components of the synthesis, such as the cross-linker, can be changed as well. For instance, spermine (polyamine with four amine groups) can be replaced with alternative polypeptides with less cationic properties for faster degradation. To ensure the feasibility of its use as a safe CT blood pool agent, more extensive studies on long-term cytotoxicity of PMNP will need to be done. Its plausibility for successful injection in human patients will also need to be investigated in the future. Sufficiently high concentration of PMNP could easily be reached for in vivo mice injection in our study. While achieving hundreds of mg/mL in payload concentration is possible for human subject injection, the viscosity and osmolarity of PMNP solutions at these levels of concentrations will need to be assessed. Finding gold, tantalum, and cerium nanoparticle formulations that are coated with surface ligands that result in higher payloads PCPP nanoparticles (i.e., hydrophilic, anionic) will be crucial, as it will decrease the amount of polymer needed in the formulation, thus subsequently decreasing the viscosity.

AuNPs have also been widely studied as an X-ray radiosensitizer due to their large X-ray interaction cross section, leading to better energy and radiation deposition for effective induction of local tumor cell death.[51,52] PMNP's ability to produce higher CT attenuation in various tube voltage settings in the keV region supports the idea that PMNP can potentially be more effective in energy deposition and therefore can act as a better radiosensitizer than AuNP.

DOI: 10.1021/acs.chemmater.9b03931
Chem. Mater. 2020, 32, 381−391

Furthermore, payload materials of multiple imaging modalities (e.g., quantum dots for fluorescence imaging and iron oxide nanoparticles for MR imaging) can be loaded in PMNP for multimodal imaging; hydrophilic drugs can be co-loaded with contrast agents for theranostics.

CONCLUSION

In summary, we developed a unique design of polymetal nanoparticles by encapsulating hydrophilic, small core nanoparticles that are made from three different contrast generating elements, gold, tantalum, and cerium, in PCPP polymer carriers. PMNP demonstrated efficient loading of hydrophilic payloads, encapsulating up to 1 mg of contrast generating materials per milligram of PCPP polymer, while maintaining its structural stability, safety and cytotoxicity, and biodegradability. We have also shown that the PMNP formulation is a robust CT contrast agent that can generate higher attenuation in both μCT and clinical CT imaging in various conditions when compared to its single payload counterparts, supporting our radioprotective garment-inspired hypothesis. Our promising results in the contrast properties of PMNP suggest that the development of platforms carrying multiple contrast generating materials can further improve CT contrast, therefore benefiting CT imaging in various biomedical applications.

ASSOCIATED CONTENT

Supporting Information

The Supporting Information is available free of charge at https://pubs.acs.org/doi/10.1021/acs.chemmater.9b03931.

> TEM images of AuPCPP, TaPCPP, CePCPP, and overloaded PMNP, assessment of payload-dependent PMNP diameter, in vitro safety and cytotoxicity of AuPCPP, TaPCPP, and CePCPP, in vitro μCT and CT images of AuPCPP, TaPCPP, and CePCPP, numerical values and statistical significance of differences in attenuation rates of PCPP formulations based on mass and molar concentration, and simulation of relative contribution from each payload element to PMNP's CT attenuation (PDF)

AUTHOR INFORMATION

Corresponding Author

*Tel.: (215) 615-4656. Fax: (240) 368-8096. E-mail: david.cormode@pennmedicine.upenn.edu.

ORCID

Johoon Kim: 0000-0002-1138-5984

Jessica C. Hsu: 0000-0002-3599-2834

David P. Cormode: 0000-0002-8391-9500

Notes

The authors declare the following competing financial interest(s): D.P.C. is named as an inventor on a patent application related to this polymeric nanoparticle formulation and owns stock in a company that has licensed this intellectual property.

ACKNOWLEDGMENTS

This work was supported by the National Institutes of Health [R01 HL131557] (D.P.C.), the American Heart Association [18PRE34030383] (J.K.), and Philips Healthcare (D.P.C.).

REFERENCES

(1) Cole, L. E.; Ross, R. D.; Tilley, J. M.; Vargo-Gogola, T.; Roeder, R. K. Gold Nanoparticles as Contrast Agents in X-ray Imaging and Computed Tomography. *Nanomedicine* **2015**, *10*, 321−341.

(2) Cormode, D. P.; Naha, P. C.; Fayad, Z. A. Nanoparticle Contrast Agents for Computed Tomography: A Focus on Micelles. *Contrast Media Mol. Imaging* **2014**, *9*, 37−52.

(3) Lee, N.; Choi, S. H.; Hyeon, T. Nano-Sized CT Contrast Agents. *Adv. Mater.* **2013**, *25*, 2641−2660.

(4) Hernandez-Rivera, M.; Kumar, I.; Cho, S. Y.; Cheong, B. Y.; Pulikkathara, M. X.; Moghaddam, S. E.; Whitmire, K. H.; Wilson, L. J. High-Performance Hybrid Bismuth-Carbon Nanotube Based Contrast Agent for X-ray CT Imaging. *ACS Appl. Mater. Interfaces* **2017**, *9* (7), 5709−5716.

(5) Liu, Y.; Liu, J.; Ai, K.; Yuan, Q.; Lu, L. Recent Advances in Ytterbium-Based Contrast Agents for In Vivo X-ray Computed Tomography Imaging: Promises and Prospects. *Contrast Media Mol. Imaging* **2014**, *9* (1), 26−36.

(6) McGinnity, T. L.; Dominguez, O.; Curtis, T. E.; Nallathamby, P. D.; Hoffman, A. J.; Roeder, R. K. Hafnia (HfO2) Nanoparticles as an X-ray Contrast Agent and Mid-Infrared Biosensor. *Nanoscale* **2016**, *8* (28), 13627−13637.

(7) Oh, M. H.; Lee, N.; Kim, H.; Park, S. P.; Piao, Y.; Lee, J.; Jun, S. W.; Moon, W. K.; Choi, S. H.; Hyeon, T. Large-Scale Synthesis of Bioinert Tantalum Oxide Nanoparticles for X-ray Computed Tomography Imaging and Bimodal Image-Guided Sentinel Lymph Node Mapping. *J. Am. Chem. Soc.* **2011**, *133*, 5508−5515.

(8) Faucon, A. L.; Bobrie, G.; Clement, O. Nephrotoxicity of Iodinated Contrast Media: From Pathophysiology to Prevention Strategies. *Eur. J. Radiol.* **2019**, *116*, 231−241.

(9) Mehran, R.; Dangas, G. D.; Weisbord, S. D. Contrast-Associated Acute Kidney Injury. *N. Engl. J. Med.* **2019**, *380*, 2146−2155.

(10) Stacul, F.; van der Molen, A. J.; Reimer, P.; Webb, J. A.; Thomsen, H. S.; Morcos, S. K.; Almen, T.; Aspelin, P.; Bellin, M. F.; Clement, O.; Heinz-Peer, G. Contrast Media Safety Committee of European Society of Urogenital, R., Contrast Induced Nephropathy: Updated ESUR Contrast Media Safety Committee Guidelines. *Eur. Radiol.* **2011**, *21*, 2527−2541.

(11) Damman, K.; Testani, J. M. The Kidney in Heart Failure: An Update. *Eur. Heart J.* **2015**, *36*, 1437−1444.

(12) Yeh, B. M.; FitzGerald, P. F.; Edic, P. M.; Lambert, J. W.; Colborn, R. E.; Marino, M. E.; Evans, P. M.; Roberts, J. C.; Wang, Z. J.; Wong, M. J.; Bonitatibus, P. J., Jr. Opportunities for New CT Contrast Agents to Maximize the Diagnostic Potential of Emerging Spectral CT Technologies. *Adv. Drug Delivery Rev.* **2017**, *113*, 201−222.

(13) Mieszawska, A. J.; Mulder, W. J.; Fayad, Z. A.; Cormode, D. P. Multifunctional Gold Nanoparticles for Diagnosis and Therapy of Disease. *Mol. Pharmaceutics* **2013**, *10*, 831−847.

(14) Al Zaki, A.; Joh, D.; Cheng, Z. L.; De Barros, A. L. B.; Kao, G.; Dorsey, J.; Tsourkas, A. Gold-Loaded Polymeric Micelles for Computed Tomography-Guided Radiation Therapy Treatment and Radiosensitization. *ACS Nano* **2014**, *8*, 104−112.

(15) Chhour, P.; Naha, P. C.; O'Neill, S. M.; Litt, H. I.; Reilly, M. P.; Ferrari, V. A.; Cormode, D. P. Labeling Monocytes with Gold Nanoparticles to Track Their Recruitment in Atherosclerosis with Computed Tomography. *Biomaterials* **2016**, *87*, 93−103.

(16) Liu, Z.; Li, Z.; Liu, J.; Gu, S.; Yuan, Q.; Ren, J.; Qu, X. Long-Circulating Er3+-Doped Yb2O3 Up-Conversion Nanoparticle as an In Vivo X-Ray CT Imaging Contrast Agent. *Biomaterials* **2012**, *33*, 6748−6757.

(17) Ahmad, M. W.; Xu, W.; Kim, S. J.; Baeck, J. S.; Chang, Y.; Bae, J. E.; Chae, K. S.; Park, J. A.; Kim, T. J.; Lee, G. H. Potential Dual Imaging Nanoparticle: Gd2O3 Nanoparticle. *Sci. Rep.* **2015**, *5*, 8549.

(18) Bonitatibus, P. J.; Torres, A. S.; Kandapallil, B.; Lee, B. D.; Goddard, G. D.; Colborn, R. E.; Marino, M. E. Preclinical Assessment of a Zwitterionic Tantalum Oxide Nanoparticle X-ray Contrast Agent. *ACS Nano* **2012**, *6*, 6650−6658.

DOI: 10.1021/acs.chemmater.9b03931
Chem. Mater. 2020, 32, 381−391

(19) Rabin, O.; Perez, J. M.; Grimm, J.; Wojtkiewicz, G.; Weissleder, R. An X-ray Computed Tomography Imaging Agent Based on Long-Circulating Bismuth Sulphide Nanoparticles. *Nat. Mater.* **2006**, *5*, 118−122.
(20) Meir, R.; Popovtzer, R. Cell Tracking Using Gold Nanoparticles and Computed Tomography Imaging. *Wiley Interdiscip. Rev. Nanomed. Nanobiotechnol.* **2018**, *10*, 1480.
(21) Kim, J.; Chhour, P.; Hsu, J.; Litt, H. I.; Ferrari, V. A.; Popovtzer, R.; Cormode, D. P. Use of Nanoparticle Contrast Agents for Cell Tracking with Computed Tomography. *Bioconjugate Chem.* **2017**, *28*, 1581−1597.
(22) Bonitatibus, P. J., Jr.; Torres, A. S.; Goddard, G. D.; FitzGerald, P. F.; Kulkarni, A. M. Synthesis, Characterization, and Computed Tomography Imaging of a Tantalum Oxide Nanoparticle Imaging Agent. *Chem. Commun. (Cambridge, U. K.)* **2010**, *46*, 8956−8958.
(23) Kim, J.; Bar-Ness, D.; Si-Mohamed, S.; Coulon, P.; Blevis, I.; Douek, P.; Cormode, reiD. P. Assessment of Candidate Elements for Development of Spectral Photon-Counting CT Specific Contrast Agents. *Sci. Rep.* **2018**, *8*, 12119.
(24) Riederer, I.; Bar-Ness, D.; Kimm, M. A.; Si-Mohamed, S.; Noël, P. B.; Rummeny, E. J.; Douek, P.; Pfeiffer, D. Liquid Embolic Agents in Spectral X-ray Photon-Counting Computed Tomography Using Tantalum K-edge Imaging. *Sci. Rep.* **2019**, *9*, 5268.
(25) Das, S.; Dowding, J. M.; Klump, K. E.; McGinnis, J. F.; Self, W.; Seal, S. Cerium Oxide Nanoparticles: Applications and Prospects in Nanomedicine. *Nanomedicine* **2013**, *8*, 1483−1508.
(26) Pirmohamed, T.; Dowding, J. M.; Singh, S.; Wasserman, B.; Heckert, E.; Karakoti, A. S.; King, J. E. S.; Seal, S.; Self, W. T. Nanoceria Exhibit Redox State-Dependent Catalase Mimetic Activity. *Chem. Commun.* **2010**, *46*, 2736−2738.
(27) Walkey, C.; Das, S.; Seal, S.; Erlichman, J.; Heckman, K.; Ghibelli, L.; Traversa, E.; McGinnis, J. F.; Self, W. T. Catalytic Properties and Biomedical Applications of Cerium Oxide Nanoparticles. *Environ. Sci.: Nano* **2015**, *2*, 33−53.
(28) Kazempour, M.; Saeedimoghadam, M.; Shekoohi Shooli, F.; Shokrpour, N. Assessment of the Radiation Attenuation Properties of Several Lead Free Composites by Monte Carlo Simulation. *J. Biomed. Eng.* **2015**, *5*, 67−76.
(29) Livingstone, R. S.; Varghese, A.; Keshava, S. N. A Study on the Use of Radiation-Protective Apron among Interventionists in Radiology. *J. Clin. Imaging Sci.* **2018**, *8*, 34.
(30) Andrianov, A. K.; Marin, A.; Martinez, A. P.; Weidman, J. L.; Fuerst, T. R. Hydrolytically Degradable PEGylated Polyelectrolyte Nanocomplexes for Protein Delivery. *Biomacromolecules* **2018**, *19*, 3467−3478.
(31) Martinez, A. P.; Qamar, B.; Fuerst, T. R.; Muro, S.; Andrianov, A. K. Biodegradable "Smart" Polyphosphazenes with Intrinsic Multifunctionality as Intracellular Protein Delivery Vehicles. *Biomacromolecules* **2017**, *18*, 2000−2011.
(32) Nukavarapu, S. P.; Kumbar, S. G.; Brown, J. L.; Krogman, N. R.; Weikel, A. L.; Hindenlang, M. D.; Nair, L. S.; Allcock, H. R.; Laurencin, C. T. Polyphosphazene/Nano-Hydroxyapatite Composite Microsphere Scaffolds for Bone Tissue Engineering. *Biomacromolecules* **2008**, *9*, 1818−1825.
(33) Kumbar, S. G.; Bhattacharyya, S.; Nukavarapu, S. P.; Khan, Y. M.; Nair, L. S.; Laurencin, C. T. In Vitro and In Vivo Characterization of Biodegradable Poly(organophosphazenes) for Biomedical Applications. *J. Inorg. Organomet. Polym. Mater.* **2007**, *16*, 365−385.
(34) Cheheltani, R.; Ezzibdeh, R. M.; Chhour, P.; Pulaparthi, K.; Kim, J.; Jurcova, M.; Hsu, J. C.; Blundell, C.; Litt, H. I.; Ferrari, V. A.; Allcock, H. R.; Sehgal, C. M.; Cormode, D. P. Tunable, Biodegradable Gold Nanoparticles as Contrast Agents for Computed Tomography and Photoacoustic Imaging. *Biomaterials* **2016**, *102*, 87−97.
(35) Asati, A.; Santra, S.; Kaittanis, C.; Nath, S.; Perez, J. M. Oxidase-Like Activity of Polymer-Coated Cerium Oxide Nanoparticles. *Angew. Chem., Int. Ed.* **2009**, *48*, 2308−2312.
(36) Sethuraman, S.; Nair, L. S.; El-Amin, S.; Farrar, R.; Nguyen, M. T.; Singh, A.; Allcock, H. R.; Greish, Y. E.; Brown, P. W.; Laurencin, C. T. In Vivo Biodegradability and Biocompatibility Evaluation of Novel Alanine Ester Based Polyphosphazenes in a Rat Model. *J. Biomed. Mater. Res., Part A* **2006**, *77*, 679−687.
(37) Bouche, M.; Puhringer, M.; Iturmendi, A.; Amirshaghaghi, A.; Tsourkas, A.; Teasdale, I.; Cormode, D. P. Activatable Hybrid Polyphosphazene-AuNP Nanoprobe for ROS Detection by Bimodal PA/CT Imaging. *ACS Appl. Mater. Interfaces* **2019**, *11*, 28648−28656.
(38) Hsu, J. C.; Naha, P. C.; Lau, K. C.; Chhour, P.; Hastings, R.; Moon, B. F.; Stein, J. M.; Witschey, W. R. T.; McDonald, E. S.; Maidment, A. D. A.; Cormode, D. P. An All-in-One Nanoparticle (AION) Contrast Agent for Breast Cancer Screening with DEM-CT-MRI-NIRF Imaging. *Nanoscale* **2018**, *10* (36), 17236−17248.
(39) Galper, M. W.; Saung, M. T.; Fuster, V.; Roessl, E.; Thran, A.; Proksa, R.; Fayad, Z. A.; Cormode, D. P. Effect of Computed Tomography Scanning Parameters on Gold Nanoparticle and Iodine Contrast. *Invest. Radiol.* **2012**, *47*, 475−481.
(40) Finkelstein, E. A.; Khavjou, O. A.; Thompson, H.; Trogdon, J. G.; Pan, L.; Sherry, B.; Dietz, W. Obesity and Severe Obesity Forecasts Through 2030. *Am. J. Prev. Med.* **2012**, *42*, 563−570.
(41) Modica, M. J.; Kanal, K. M.; Gunn, M. L. The Obese Emergency Patient: Imaging Challenges and Solutions. *Radiographics* **2011**, *31*, 811−823.
(42) Chen, H.; Danielsson, M.; Xu, C. Size-Dependent Scanning Parameters (kVp and mAs) for Photon-Counting Spectral CT System in Pediatric Imaging: Simulation Study. *Phys. Med. Biol.* **2016**, *61*, 4105−4126.
(43) Cormode, D. P.; Roessl, E.; Thran, A.; Skajaa, T.; Gordon, R. E.; Schlomka, J. P.; Fuster, V.; Fisher, E. A.; Mulder, W. J.; Proksa, R.; Fayad, Z. A. Atherosclerotic Plaque Composition: Analysis with Multicolor CT and Targeted Gold Nanoparticles. *Radiology* **2010**, *256*, 774−782.
(44) Geng, J.; Li, K.; Pu, K. Y.; Ding, D.; Liu, B. Conjugated Polymer and Gold Nanoparticle Co-loaded PLGA Nanocomposites with Eccentric Internal Nanostructure for Dual-Modal Targeted Cellular Imaging. *Small* **2012**, *8*, 2421−2429.
(45) Hua, H.; Zhang, N.; Liu, D.; Song, L.; Liu, T.; Li, S.; Zhao, Y. Multifunctional Gold Nanorods and Docetaxel-Encapsulated Liposomes for Combined Thermo- and Chemotherapy. *Int. J. Nanomed.* **2017**, *12*, 7869−7884.
(46) Huang, C. H.; Nwe, K.; Al Zaki, A.; Brechbiel, M. W.; Tsourkas, A. Biodegradable Polydisulfide Dendrimer Nanoclusters as MRI Contrast Agents. *ACS Nano* **2012**, *6*, 9416−9424.
(47) Kim, J.; Arifin, D. R.; Muja, N.; Kim, T.; Gilad, A. A.; Kim, H.; Arepally, A.; Hyeon, T.; Bulte, J. W. Multifunctional Capsule-In-Capsules for Immunoprotection and Trimodal Imaging. *Angew. Chem., Int. Ed.* **2011**, *50*, 2317−2321.
(48) Pan, D.; Roessl, E.; Schlomka, J. P.; Caruthers, S. D.; Senpan, A.; Scott, M. J.; Allen, J. S.; Zhang, H.; Hu, G.; Gaffney, P. J.; Choi, E. T.; Rasche, V.; Wickline, S. A.; Proksa, R.; Lanza, G. M. Computed Tomography in Color: NanoK-Enhanced Spectral CT Molecular Imaging. *Angew. Chem., Int. Ed.* **2010**, *49*, 9635−9639.
(49) Chhour, P.; Gallo, N.; Cheheltani, R.; Williams, D.; Al-Zaki, A.; Paik, T.; Nichol, J. L.; Tian, Z. C.; Naha, P. C.; Witschey, W. R.; Allcock, H. R.; Murray, C. B.; Tsourkas, A.; Cormode, D. P. Nanodisco Balls: Control over Surface Versus Core Loading of Diagnostically Active Nanocrystals into Polymer Nanoparticles. *ACS Nano* **2014**, *8*, 9143−9153.
(50) Allcock, H. R. Recent Developments in Polyphosphazene Materials Science. *Curr. Opin. Solid State Mater. Sci.* **2006**, *10*, 231−240.
(51) Haume, K.; Rosa, S.; Grellet, S.; Smialek, M. A.; Butterworth, K. T.; Solov'yov, A. V.; Prise, K. M.; Golding, J.; Mason, N. J. Gold Nanoparticles for Cancer Radiotherapy: A Review. *Cancer Nanotechnol.* **2016**, *7*, 8.
(52) Her, S.; Jaffray, D. A.; Allen, C. Gold Nanoparticles for Applications in Cancer Radiotherapy: Mechanisms and Recent Advancements. *Adv. Drug Delivery Rev.* **2017**, *109*, 84−101.

DOI: 10.1021/acs.chemmater.9b03931
Chem. Mater. 2020, 32, 381−391